PHYSICS

Observation of electron-induced characteristic x-ray and bremsstrahlung radiation from a waveguide cavity

Malte Vassholz and Tim Salditt*

We demonstrate x-ray generation based on direct emission of spontaneous x-rays into waveguide modes. Photons are generated by electron impact onto a structured anode target, which is formed as an x-ray waveguide or waveguide array. Both emission of characteristic radiation and bremsstrahlung are affected by the changes in mode density induced by the waveguide structure. We investigate how the excited modal pattern depends on the positions of the metal atoms and the distance of the focused electron beam with respect to the waveguide exit side. We compare the results to synchrotron-excited fluorescence. We then discuss how x-ray generation in waveguides can be used to increase the brilliance and directional emission of tabletop x-ray sources, with a corresponding increase in the spatial coherence. On the basis of the Purcell effect, we lastly show that the gain of emission into waveguide modes is governed by the quality factor of the waveguide.

INTRODUCTION

X-ray generation at the laboratory scale largely relies on electron impact sources and generation of characteristic x-ray radiation or bremsstrahlung in metal anodes. The continuous development of these sources has spurred fundamental science, particularly structure analysis by crystallography and x-ray diffraction, and benefits everyday applications of medical imaging or nondestructive testing (*1*).

The recent increase in brightness by μ-focus sources and especially liquid jet anodes (*2*, *3*) now enables new applications by phase-contrast imaging and high-resolution diffraction. Notwithstanding this progress, the principles of x-ray emission after K-shell ionization or by bremsstrahlung interaction in an anode have been the same over the past 120 years. In particular, the fact that nonrelativistic electron impact sources emit x-ray photons into the entire solid angle of 4π sr, with only smooth modulations due to polarization and self-absorption effects, severely limits their brightness [e.g., ph/(mm^2·sr·s), where ph denotes photons]. Collecting photons over a wide angular range and refocusing them onto a sample is hampered by the fact that the x-ray index of refraction $n = 1 - \delta + i\beta$ asymptotically approaches one for high photon energy E. Resonators with sufficient quality factor Q to exploit effects of cavity quantum electrodynamics, for example, seem to be out of reach for broadband laboratory radiation. Cavities based on dynamic single-crystal reflection, for example, can be operated only for extremely narrow-banded radiation, making synchrotron radiation indispensable (*4*–*7*). This is in sharp contrast to visible light, where the spontaneous emission is easily modified, already by placing the emitting molecule near a single interface (*8*). When incorporated into a suitable resonator, spontaneous emission can be suppressed or enhanced, known as the Purcell effect (*9*), by many orders of magnitude. Changes in the modal density by structured matter are, in principle, also known for x-rays since the discovery of the Kossel effect in single-crystal anodes (*10*), and as an extension, angular modulations of x-ray fluorescence are also commonly observed in thin films and multilayers, both for excitation with synchrotron radiation and electrons (*11*–*13*), including the regime of relativistic electrons (*14*). These effects have also been discussed in view of possible use for x-ray lasers (*13*).

A much stronger modification of the modal density, however, can be provided by waveguides. Waveguiding becomes possible for x-rays by total reflection at grazing angles within suitable thin-film structures (*15*–*19*) or in two-dimensional channel waveguides (*20*–*22*), which can, in principle, offer much higher Q. In the simplest case, a planar guiding layer can be formed, for example, by a thin film with low electron density, surrounded by a high electron density cladding, enabling beam confinement down to sub–10 nm full width at half maximum (FWHM) (*23*). Planar x-ray waveguides have already been used for fundamental x-ray quantum optics experiments in nuclear resonant scattering, e.g., measurements of increased spontaneous emission of atoms in a cavity (*24*), the collective Lamb shift of a cavity mode (*25*), electromagnetically induced transparency (*26*), the collective strong coupling of x-rays and nuclei (*27*), as well as for coupling to electronic resonances (*28*). These x-ray quantum optics experiments as well as coherent imaging with waveguide modes (*29*) rely on the coupling of highly brilliant synchrotron radiation into x-ray waveguides. While feasible for synchrotron radiation, this sequential approach of first generating x-rays and then coupling them into a waveguide is unsuited for laboratory x-ray radiation because of the low brilliance of electron impact sources. For this reason, waveguide optics is largely irrelevant for laboratory x-ray radiation today.

In this work, we present evidence for direct emission of characteristic and bremsstrahlung radiation into a waveguide. We directly generate x-rays inside a waveguide by a μ-focus electron beam (e-beam). This is fundamentally different from first generating the x-rays and then coupling into the waveguide, even if done in close proximity as in (*30*), and results in pronounced peaks in the angular far-field distribution. Hence, x-ray emission into waveguide modes not only is of interest in view of x-ray quantum optics but also could augment the performance of electron impact sources since waveguides with $Q \gg 1$ could be exploited for a correspondingly increased spatial coherence. Furthermore, we show that the distance Δz between the spot of electron impact and waveguide exit can be used to control the far-field emission pattern. Last, we compare the measured far-field distribution to waveguide emission of x-ray fluorescence excited by synchrotron radiation, which we measure for the same waveguides, again with a precise control of Δz.

Institut für Röntgenphysik, Georg-August-Universität Göttingen, Friedrich-Hund-Platz 1, Göttingen, Germany.
*Corresponding author. Email: tsaldit@gwdg.de

RESULTS

Experimental setup

To excite characteristic and bremsstrahlung radiation by electron bombardment inside the waveguide structures, we used the e-beam and electron optics of a modified μ-focus x-ray tube (R5 prototype, Excillum AB). A custom anode chamber design allowed the mounting of a planar waveguide structure on a grounded metal support. A main control parameter was the distance Δz between the exit side of the waveguide structure and the point of x-ray generation (Fig. 1A), i.e., the position of the electron spot, which was varied by adapting the current in the deflection coils. The e-beam was focused to a spot size of 10 μm FWHM. We varied the acceleration voltage between 15 and 50 kV with a total e-beam power of 400 to 450 mW. A silicon drift detector (SDD) resolved the x-rays outside the anode chamber as a function of photon energy E and angle θ_f with respect to the waveguide horizon (Fig. 1A). For an increased angular resolution $\Delta\theta_f$ of the detection angle, the SDD detector can be replaced by the charge-integrative hybrid pixel detector MÖNCH (MÖNCH03 prototype, Paul Scherrer Institut) (*31*). Inside the waveguide anode, the x-rays are generated (Fig. 1A) either in a small, nearly monoatomic layer [fluorescent metal layer (FL)] within the low-density guiding layer and/or inside the metal cladding layer. The x-rays generated within a region enveloped within a waveguide mode can couple into the mode, regardless of whether the metal is contained in the fluorescent layer, dispersed in the guiding layer, or contained in the cladding layer. The latter is of practical importance since the high-density cladding is almost always composed of metal atoms.

X-rays that are emitted into the waveguide modes can exit either through the top for the case of a leaky waveguide design based on a thin top cladding or after propagation in the guiding layer at the exit side, i.e., at the truncation of the thin-film structure (Fig. 1B). The recorded intensity patterns (Fig. 1C) are interpreted with respect to the simulated modes of the waveguide, with their characteristic nodes and antinodes. For comparison, we excited x-ray–induced fluorescence with a tabletop μ-focus x-ray tube and synchrotron radiation. The observation angle of the x-ray fluorescence was at 90° to the primary x-ray beam (see Fig. 1A). The synchrotron setup was the GINIX endstation (*32*) at the beamline P10 (PETRA III, DESY). The synchrotron beam was focused to submicrometer spot size by a Kirkpatrick-Baez mirror system. Details of all setups, instrumentation, and parameters used are given in Methods.

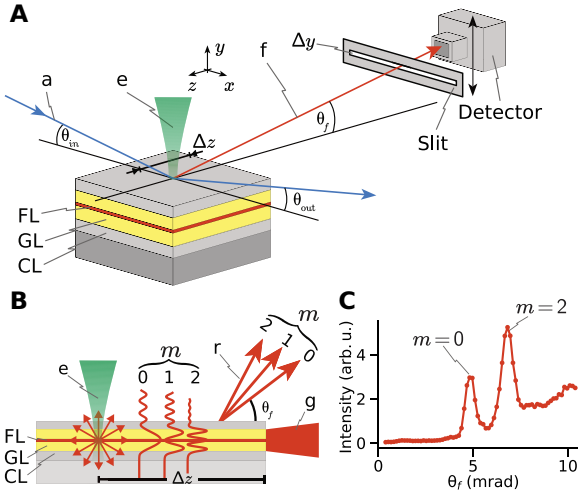

Fig. 1. X-ray generation in waveguides. (**A**) An e-beam (e) impinges onto a planar waveguide consisting of cladding layer (CL), guiding layer (GL), and a central fluorescent metal layer (FL). The electron impact excites atoms, which emit characteristic x-rays and bremsstrahlung into the waveguide. Angle- and energy-resolved detection is implemented by scanning an SDD detector. To increase the angular resolution, the SDD can be replaced by the MÖNCH detector. For excitation with x-rays: The e-beam (e) is replaced by a focused x-ray beam (a) impinging the waveguide in grazing incidence. Here, the detection is in an angle of 90° to the primary x-ray beam. Both beams (e) and (a) can be scanned in Δz to change the propagation length of the generated x-rays inside the waveguide. (**B**) Detailed view on the x-ray generation with electron impact. Characteristic x-rays are emitted into waveguide modes with mode numbers m. The x-rays exit the channel either through the thinned top cladding by evanescent waves (r) or directly at the end of the channel (g). (**C**) Detected far-field emission of characteristic x-rays generated inside the waveguide shows sharp emission peaks at the structure's horizon.

Samples

We performed experiments with three different planar waveguide systems, to which we will refer as Cu/Co, Fe/Ni, and Mo/C system. The exact layer compositions are given in Table 1. The Cu/Co system is a single waveguide with a small nearly monoatomic layer (∂-layer) of Co in the C guiding layer sandwiched between Cu cladding layers. The thin top cladding allows for resonant beam coupling (RBC) into and out of the guided modes from the top interface. The two other systems are multiwaveguide systems, i.e., waveguides with multiple guiding layers. The Fe/Ni system is a 50× stack of waveguides with a small ∂-layer of Fe in the center of the C guiding layer, sandwiched between Ni cladding. The Mo/C multiwaveguide system contains 30 waveguides with a ∂-layer of Mo in the center of the C guiding layers. The thick Mo cladding layers suppress RBC and thus reduce x-rays, leaving the channel through the top of the waveguide. Further details on the sample preparation are given in Methods.

The three systems were chosen to investigate several different metal compositions and geometric designs. While two systems allow the separation of fluorescent layer and cladding layer contributions, the Mo/C multiwaveguide system is designed in view of higher signal with cladding layer and fluorescent layer emitting at

Table 1. Waveguide samples. The layer composition of the three samples is listed from top to bottom.

Sample	Cu/Co	Fe/Ni	Mo/C
Top layers	1× { Cu, 5 nm; C, 20 nm; Co, 2 nm; C, 20 nm }	50× { Ni, 10 nm; C, 24.5 nm; Fe, 1 nm; C, 24.5 nm }	30× { Mo, 25 nm; C, 16 nm; Mo, 1 nm; C, 16 nm }
Bottom layer	Cu, 40 nm	Ni, 30 nm	Mo, 30 nm
Buffer layer	–	–	Cr, 10 nm
Substrate	Si	Si	Si
Fabrication process	Pulsed laser deposition	Magnetron sputtering	Magnetron sputtering

the same energy. The concept of amplification by waveguide multilayers is also particularly relevant for future upscaling. Note that for most applications, it is not necessary to separate the emission of different layers, as they would all emit into the same radiation cone.

Simulations

We simulated the x-ray generation inside the waveguides based on the reciprocity theorem. Accordingly, the simulation process is inverted to the experimental conditions. Instead of asking for the far-field probability distribution of a photon emitted from the location of a metal atom into a waveguide mode, propagating through the guide, and then leaving through the thinned top cladding or the side face, we ask for the field intensity at a given metal location inside the waveguide, when a far-field solution, i.e., a plane wave, impinges onto the structure (Fig. 2). If the excitation is far from the waveguide's exit face and the radiation can enter and exit only through the cladding (i.e., large Δz), the calculation of the wavefield inside the guides can be carried out for semi-infinite media and beams by matrix methods (Parratt) (*33*). To describe the Δz dependence as required for the measurements close to the exit side at small Δz, we have used a finite-difference propagation code (*34*), taking into account the finite size and, if needed, the full dimensionality of the structure. We have verified that for semi-infinite systems and infinite beams, the two simulation approaches (finite difference and Parratt) give identical results. Figure 2A shows the spatial intensity distribution inside a single waveguide channel with the same layer composition as the Mo/C multiwaveguide system. The intensity of the propagated field was calculated by finite-difference simulations (*34*). The internal intensity distribution in the *yz* plane is shown for different plane wave angles of incidence θ_{PW}, each matching a different mode. In terms of the reciprocity theorem, the maps indicate the probability that a photon emitted at the given location exits to the corresponding far-field angle θ_f. Note the symmetries of the modes along *y* and the breaking of translational symmetry invariance along *z* that is induced by the truncation of the waveguide (exit side). Figure 2B shows the intensity variation in the central metal layer with peaks corresponding to the modes. The broad maximum at $\theta_{PW} \simeq 0$ corresponds to side coupling. As an interesting interference phenomenon, if one "moves" an excited atom along *z* in the cavity, the emission rate into a waveguide mode oscillates with *z*, i.e., with the distance Δz to the exit side. This effect highlights that the emission into specific modes is modified by both dimensions of the waveguide structure. While the interpretation in terms of modal propagation is comparably simple for a structure with a single waveguide, the interference effects when simulated for the multiwaveguide system become both more complex and much more pronounced.

Experimental results

Figure 3 shows the recorded far-field patterns of the characteristic Co and Cu radiation for the Co/Cu waveguide excited by electron bombardment and, for comparison, also fluorescence induced by a laboratory μ-focus x-ray source for the same sample structure. The data were recorded by the SDD detector with an angular resolution of $\Delta\theta_f = 250$ μrad for x-ray–induced fluorescence and $\Delta\theta_f = 285$ μrad for electron impact. The Co-K radiation, which is excited in the central ∂-layer, couples preferably to the even modes of the waveguide cavity, namely, $m = 0$ and $m = 2$ with antinodes in the central Co layer (Fig. 3A for Co-K_α and fig. S1 for Co-K_β). For the e-beam–excited characteristic radiation, the radiant flux Φ_p per e-beam power [ph/(s·mrad^2·W)] is given on the right ordinate. The modal pattern of the Cu-K_α radiation, excited in the cladding, peaks at even and uneven modes, as expected since all modes exhibit strong evanescent tails in the cladding (Fig. 3B). For the signal detected from both layers, electron and x-ray excitation show similar patterns. The peak positions agree with the simulations. For better comparability, we have convolved the angular distribution of the simulated data with the instrumental resolution of $\Delta\theta_f = 250$ μrad. Synchrotron-excited fluorescence of this structure with higher angular resolution and where the radiation exits through the side edge of the waveguide are shown in fig. S2.

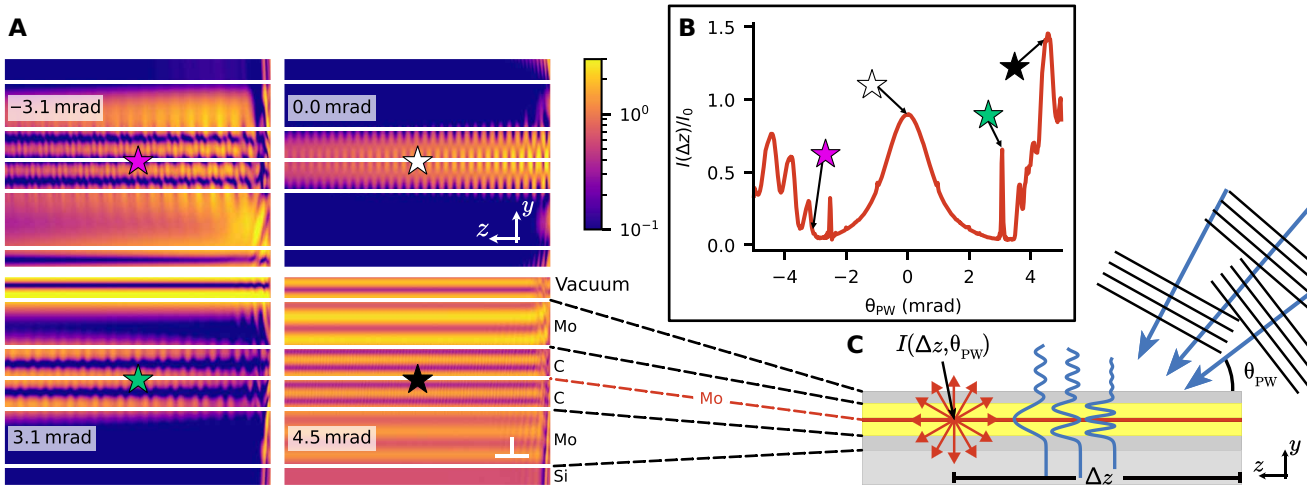

Fig. 2. Simulation of propagation and modal emission. (**A**) Propagation of the electric field inside a single Mo/C waveguide, when a plane wave is incident under the angle θ_{PW} as given in the inset. The main direction of propagation is along the *z* direction [see (**C**)]. The propagation is based on finite-difference simulations. (**B**) Intensity of the propagated field as a function of θ_{PW} in the center of the guiding layer and at a distance of $\Delta z = 400$ μm to the side edge. The colored stars mark the positions in (A) and (B). According to the reciprocity theorem, we now change directions: If an atom in the center of the guiding layer and at a distance of $\Delta z = 400$ μm emits x-rays, then the intensity measured at an angle $\theta_f = \theta_{PW}$ is given by (B). Scale bars (A), 10 nm in *y* and 100 μm in *z*. The color in (A) scales with the normalized intensity of the electric field on a logarithmic scale.

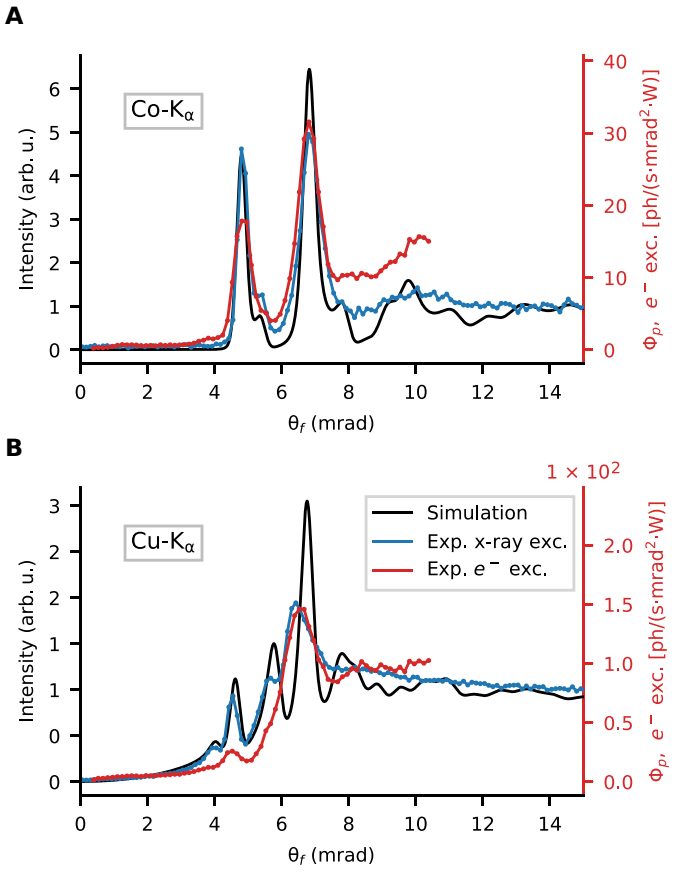

Fig. 3. Characteristic radiation in the Co/Cu waveguide. Far-field intensity of the characteristic K_α lines, exhibiting modal peaks as a function of angle θ_f with respect to the waveguide horizon. Intensities measured with an SDD detector excited with electron impact and, for comparison, fluorescence excited with a laboratory x-ray tube. The right ordinate shows the K_α radiant flux Φ_p per e-beam power for the characteristic (e-beam excited) radiation. (**A**) Co-K_α radiation excited in the central ∂-layer. (**B**) Cu-K_α radiation excited in the cladding. Peak positions match the simulated intensities.

To investigate the emission of x-rays into multiwaveguides, we first turn to synchrotron-excited fluorescence inside the Fe/Ni multiwaveguide system before investigating this effect for characteristic radiation generated by electron bombardment. The synchrotron setup has two advantages for the interpretation of the experimental data: (i) The monochromatic 8-keV beam allows for the excitation of the central Fe layers only, whereas the K-edge of the Ni cladding layers is above the primary photon energy. (ii) The nanofocused synchrotron beam excites a small region only, such that the distance Δz to the side edge of the waveguide structure is well controllable with negligible primary beam size. Figure 4A shows the Fe-K signal of an exemplary detector image of the MÖNCH. By interpixel interpolation of the MÖNCH, we obtain a sampling corresponding to $\Delta\theta \simeq 25$ µrad. The signal shows strong modulations along the θ_f direction. Along the $\theta_\perp$ direction, perpendicular to θ_f, the intensity is constant, as expected because of the planar geometry. By integration over the horizontal extent (along $\theta_\perp$) of the detector, we obtain the intensity curve $I_{Fe}(\theta_f)$ (Fig. 4B). Fluorescence photons trapped in a waveguide mode can either leak out via an evanescent wave to the top (the equivalent of RBC) or at the side face of the waveguide (the equivalent of front coupling). The second fraction of fluorescence radiation results in an interference pattern near the horizon and is emitted from an effective source of small cross section with high divergence, controlled by the waveguide structure, i.e., mainly the guiding layer thickness. Both beams are spatially coherent; hence, the fraction leaking through the top originates from a large source spot and has low divergence (*35*).

By scanning the synchrotron beam toward the edge of the waveguide, we obtain for each position Δz an intensity curve $I_{Fe}(\theta_f)$. Figure 4C shows these curves as an intensity map $I_{Fe}(\theta_f, \Delta z)$. The intensity map highlights the periodicity in Δz of the radiation exiting at the side face of the waveguide ($\theta_f \simeq 0$). The modal structure, which we already observed for the single waveguide (c.f. Fig. 3), appears again for radiation "leaking" through the top but is now modified by multiwaveguide interference. Note the pronounced interference effects at the truncated side face of the waveguide structure. Figure 4D shows simulated data for comparison.

As we show next, the strong modulation effects of x-ray emission in truncated waveguide arrays can also be exploited for characteristic radiation with electron impact sources. For the generation of characteristic x-rays with electron impact inside multiwaveguides, we chose the Mo/C structure. The 25-nm-thick Mo cladding suppresses radiation leaking evanescently through the top cladding and thus enhances the fraction of radiation exiting at the edge of the waveguide structure. Furthermore, the cladding and the central metal layer contribute to the same characteristic lines. We used the MÖNCH area detector with 4× subpixel interpolation, resulting in an angular resolution of $\Delta\theta_f \simeq 25$ µrad. A 35-µm-thick Ag foil was used as spectral filter to enhance the contrast between the bremsstrahlung background and characteristic Mo-K emission. Since the e-beam spot is substantially larger than the focused synchrotron beam, we expect the intensity modulations along Δz to be less sharp than in the synchrotron measurements. We have used the Monte Carlo software package PENELOPE2014 (*36*) to simulate the electron dose distribution in the structure for a given acceleration voltage, verifying that the e-beam reached deep into the buried waveguide structure. Figure 5A shows the Mo-K radiation as a function of angle θ_f and distance Δz, recorded by scanning the e-beam over the Mo/C waveguide target along z. Figure 5B shows the intensity exiting through the side face of the channels (integrated intensity within $|\theta_f| \leq 2.9$ mrad; c.f. green rectangle in Fig. 5A) in terms of radiant flux Φ_p per unit e-beam power for characteristic Mo-K emission. A biexponential decay Φ_p^{fit} is fitted to Φ_p to determine the characteristic decay lengths $\Delta z_{1/e}$ of the intensity inside the waveguides. The least square fit yields a slow decay with $\Delta z_{1/e} = 622(11)$ µm and a fast decay with 82(2) µm. The slow decay can be attributed to the damping of the 0th mode ($m = 0$), whereas the fast decay can be attributed to the 1st mode ($m = 1$), with a higher fraction of the modal intensity in the cladding and, thus, stronger absorption. We can estimate an effective x-ray source spot of $A_{x-ray} \simeq 9.9$ µm^2 for the radiation leaving through the side face of the waveguides, given by the guiding layer thickness times the number of waveguides 33 nm × 30 in the y direction and the width of the e-beam of 10 µm in the lateral direction. Dividing Φ_p by A_{x-ray} yields the brilliance B_p of the Mo-K radiation leaving through the waveguide's side edge per e-beam power (c.f. right ordinate in Fig. 5B). To improve the visibility for the interference effects of the radiation leaving the waveguide array at the side face, we have corrected the intensity map $I(\theta_f, \Delta z)$ in Fig. 5A for the absorption inside the channel, i.e., by division with the biexponential fit Φ_p^{fit}. The intensity leaving through the side face shows strong modulations with Δz. The modulations are not only a redistribution

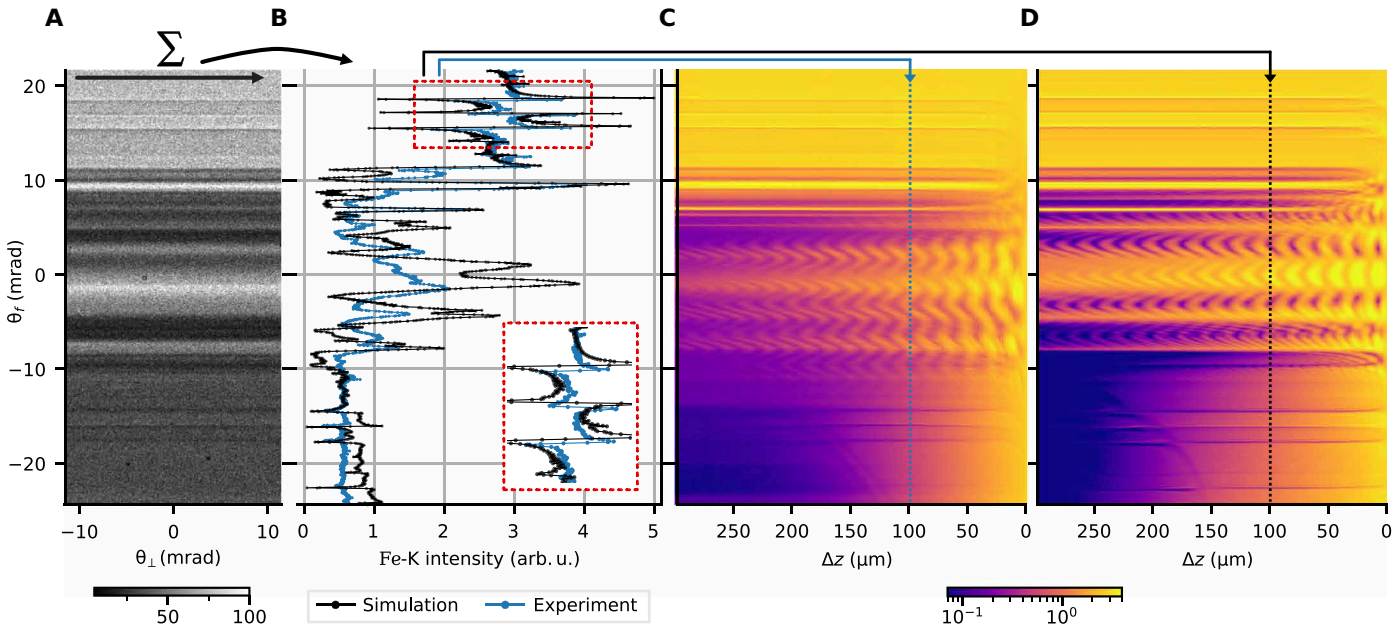

Fig. 4. Synchrotron-excited fluorescence inside the Fe/Ni multiwaveguide. Modification of Fe-K fluorescence intensity I_{Fe} by the waveguide modes, measured by scanning a focused synchrotron beam close to the side face of the waveguide. (**A**) Detector image of I_{Fe} shows strong modulations as a function of θ_f, whereas I_{Fe} is constant along the lateral direction $\theta_\perp$. Radiation exits through both interfaces: the exit face of the waveguide $\theta_f \simeq 0$ and the top cladding. The intensity at negative θ_f is damped by absorption in the substrate. (**B**) $I_{Fe}(\theta_f)$ is obtained after integration along $\theta_\perp$ of the detected intensity. The simulated intensity is shown for comparison. The zoom in the inset shows Fano-like line shapes. (**C**) The variation of fluorescence intensity close to the exit side $I_{Fe}(\theta_f, \Delta z)$, with each column of the matrix corresponding to an intensity profile such as in (B). Pronounced oscillations show that the emission of fluorescence oscillates with distance to the exit of the waveguide. (**D**) Simulated intensity. The arrows indicate Δz of the profiles shown in (B). The color scales with the intensity in arbitrary units on a linear scale (A) and logarithmic scale (C and D).

of intensity to different angles θ_f but also visible as small oscillations in the radiant flux Φ_p (c.f. Fig. 5B). Figure S3 shows Φ_p divided by Φ_p^{fit} to highlight these oscillations for different integration ranges in θ_f. For angles of $|\theta_f| \geq 4$ mrad, Fano-like intensity modulations are visible. In fig. S4, similar measurements are shown for characteristic Ni-K radiation excited in the cladding of the Fe/Ni multiwaveguide system for experimental and simulated data.

Last, we show that the observed effects of electron impact x-ray generation in waveguides not only are limited to characteristic radiation but also change the phase-space distribution for bremsstrahlung. To this end, we inspected energy-dispersive data of the SDD detector for the Fe/Ni multiwaveguide system excited with electron bombardment. The energy-resolved intensity map $I(\theta_f, E)$ (Fig. 6) shows the characteristic Fe and Ni radiation as horizontal lines, with local maxima at the external angles of the waveguide modes. In between these horizontal lines, the bremsstrahlung background shows the same local maxima, all lying on hyperbolic functions, which describe the external angles of the waveguide modes as a function of E (see inset in Fig. 6). This shows that not only characteristic radiation but also the bremsstrahlung continuum is directly emitted into the waveguide modes.

DISCUSSION

The results show that waveguide anodes affect the emission phase space of characteristic x-rays and bremsstrahlung. The far-field distribution of the emission changes with the distance between the exciting e-beam and the side edge of the waveguide. The observed intensity profiles are highly modulated with sharp features that are in good agreement with simulations based on finite differences and the reciprocity theorem. Notably, the angular emission profile of the fluorescence and characteristic radiation excited in the waveguide (c.f. Figs. 4, B to D, and 5A) exhibits a Fano-like line shape, which can be attributed to the interference of the radiation of the waveguide modes ("narrow" resonance) with fluorescence that did not couple into the waveguide (forming a "broad" background channel). The Fano line shape parameter changes as a function of the phase shift between the two contributions with θ_f, as observed for nuclear resonant scattering (*37*), giving rise to a sequence of different line shape features: Lorentzian, inverted Lorentzian, and Fano profile with cusp/dip or dip/cusp, respectively, as described in general and in great detail in (*38*).

For the Mo/C waveguide system, we have already achieved a brightness of $B_p \approx 5 \times 10^8$ ph s^{-1} mrad^{-2} mm^{-2} W^{-1}, with an experimental setup, which was not at all optimized for high brightness. We will next discuss how the brightness can be increased experimentally.

For conventional x-ray sources, the effective size of the x-ray source spot is directly proportional to the size of the e-beam. However, the source spot of the radiation generated in an x-ray waveguide and leaving the waveguide through the side face does not depend on the size of the e-beam in the z direction but only on the waveguide's geometry. Hence, an elongation of the e-beam along z with constant area power density will increase the radiant flux without increase of the effective x-ray source spot and hence will directly benefit brilliance. We have calculated this brilliance increase for the Mo/C waveguide. To this end, we numerically integrated the brilliance $B_p(\Delta z)$ shown in Fig. 5B for a given range of Δz. Figure 7 shows the resulting brilliance. Note that the area power density does not change with increasing e-beam size z_e. For z_e = 700 μm, we obtain a Mo-K

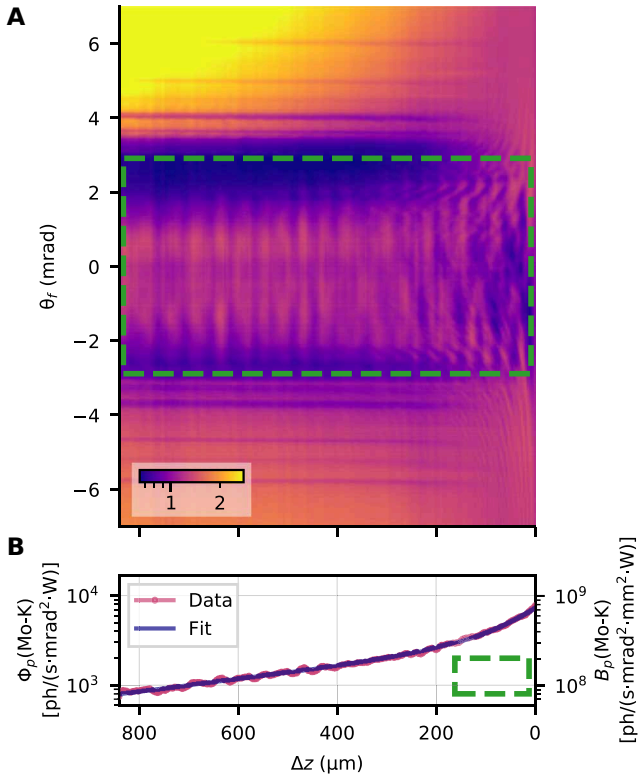

Fig. 5. Characteristic radiation of the Mo/C multiwaveguide. Variation of characteristic Mo-K intensity when scanning the e-beam toward the truncated side of the waveguide array. (**A**) I_{Mo} as a function of the exit angle θ_f and the distance Δz between the e-beam position and the waveguide edge. For better visibility of the interference effects of the radiation exiting through the side edge, the intensity map $I_{Mo}(\theta_f, \Delta z)$ has been corrected for the damping of the waveguide, by a division with Φ_p^{fit} (see below). (**B**) Total radiant flux Φ_p per incident e-beam power of Mo-K radiation exiting through the side face of the waveguide, i.e., between the angular range $|\theta_f| \leq 2.9$ mrad [green rectangle in (A)]. The least square fit Φ_p^{fit} of a biexponential decay to the radiant flux Φ_p yields two characteristic decay lengths (1/*e*-lengths), a slow decay $\Delta z_{1/e} = 622(11)$ μm and a faster decay $\Delta z_{1/e} = 82(2)$ μm, which can be attributed to the 0th and 1st mode, respectively. The right ordinate shows the Mo-K brilliance per e-beam power of the radiation leaving through the side edge. The color in (A) scales with the intensity in arbitrary units on a logarithmic scale.

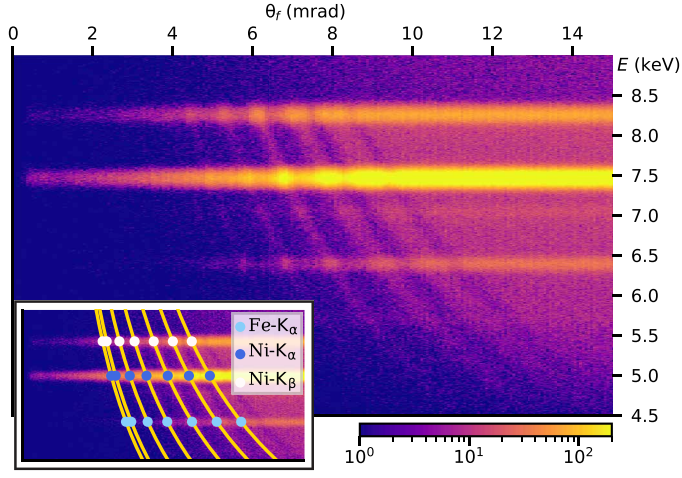

Fig. 6. E-beam–excited characteristic and bremsstrahlung radiation in the Fe/Ni multiwaveguide system. The x-ray spectrum is measured with the SDD detector as a function of exit angle θ_f. The mode pattern for each of the characteristic emission lines—Fe-K_α, Fe-K_β, Ni-K_α, and Ni-K_β—is observed as horizontal lines with the local maxima at the angles of the waveguide modes. The bremsstrahlung background in between the horizontal lines of characteristic radiation also shows the modulation of the waveguide's mode pattern. The inset shows the theoretical positions of the modes for the characteristic radiation (dots) and for the bremsstrahlung continuum (lines), with mode numbers $m = 0$ to 6 (from left to right). The color scales with the intensity in arbitrary units on a logarithmic scale.

brilliance of $B \approx 5 \times 10^9$ ph s^{-1} mrad^{-2}mm^{-2} at an area power density of 4 kW mm^{-2} of the e-beam. This area power density was chosen to be deliberately low to not saturate the MÖNCH detector (a flux as low as ~1 photon per 100 pixel and frame is required for energy-resolved detection) and is substantially lower than the damage threshold. With proper heat management, a two orders of magnitude higher power density could be applied to the waveguide target, resulting in a brilliance increase to $B \approx 5 \times 10^{11}$ ph s^{-1} mrad^{-2}mm^{-2}. To increase heat dissipation, the Si substrate of the waveguides could easily be replaced by diamond wafers with substantial increase in heat conductivity.

Next, we discuss the changes in emission, when an atom is placed in a waveguide resonator. Figure 5B indicates that a variation of Δz substantially changes the far-field distribution of the radiation emitted through the side face of the waveguide. Apart from damping due to mode propagation, small oscillations are observed, which do not vanish after integrating the intensity spectrum along θ_f (c.f. fig. S3 for a detailed presentation). Together with the rich interference profiles as a function of angle and position in the resonator, this supports the view that the emission process itself is already modified by the emitter position in the cavity. This is conceptually similar to the emission of Mössbauer atoms in thin-film structures, which have already been described successfully in the framework of cavity quantum electrodynamics (*39*). Hence, the Purcell effect describing the enhancement of the spontaneous photon emission of atoms in a cavity is the natural starting point for this problem. For a 3d cavity, the enhancement factor with respect to free space emission is given by (*9*)

$$F_P = \frac{3}{4\pi^2}\left(\frac{\lambda}{n}\right)^3 \frac{Q}{V} \quad (1)$$

where Q is the quality factor of the resonator, V is the modal volume, n is the index of refraction, and λ is the wavelength. Note that the Purcell effect can also be calculated on the basis of the reciprocity approach, as recently shown theoretically for emission from a source inside a resonator into an open optical system (*40*). In the following, we sketch out a simple argument of how to estimate the gain factor G for a source where the anode is structured such that it supports photon emission into bound modes, for example, in the form of a planar waveguide or an array of cylindrical fibers. The metal for emission of characteristic radiation can be a component of the cladding or can be integrated into the guiding core. The simplest structure would be an array of planar waveguides deposited onto a substrate, which could be used either in transmission or in reflection (Fig. 8C), as it was used in this manuscript. More challenging to fabricate, but leading to a higher G, would be an array of channel waveguides (Fig. 8B), formed for example, by macroscopically long cylindrical holes with radius $a \simeq 50$ to 200 nm etched into a metal. Starting from Fermi's golden rule for the transition rate of spontaneous emission

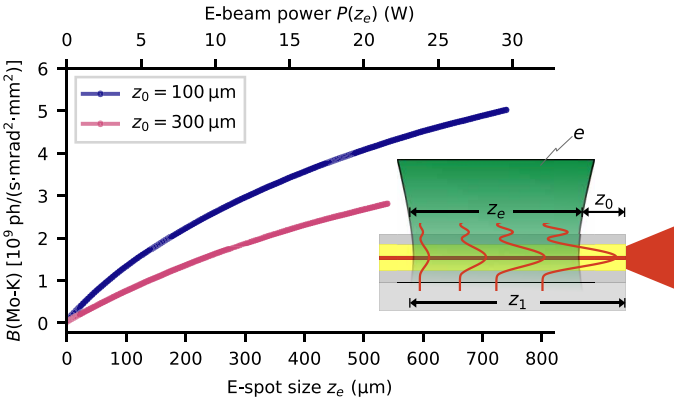

Fig. 7. Increasing the brilliance of the Mo/C waveguide with elongated e-beam spots. The brilliance B of the characteristic Mo-K radiation generated inside the Mo/C waveguide system can be increased substantially by expanding the e-beam spot on top of the waveguide along the z direction. The area power density of the e-beam is kept constant at the value used in the experiments p_e = 4kW/mm². We calculated the brilliance by numerical integration of the data in Fig. 5B. The integration limits of the e-beam are from z_0 to $z_1 = z_0 + z_e$ (see inset). Note that the effective x-ray spot size of the modes leaving the waveguide through the side face does not change with a variation of z_e. The e-beam power $P(z_e)$ is given on the upper abscissa.

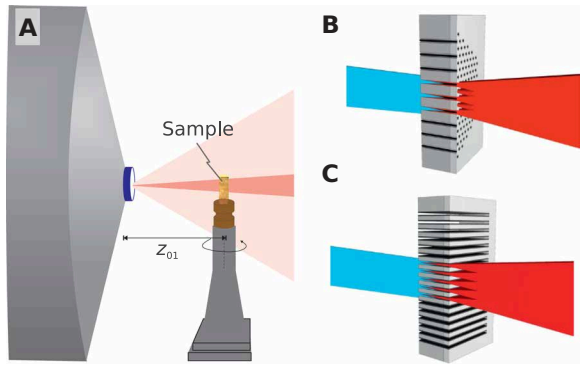

Fig. 8. X-ray source based on direct emission into waveguide modes. (**A**) A source can, for example, be realized by exchanging the conventional diamond-supported W layer in transmission targets with a diamond-supported waveguide structure. The waveguide anode emits into a narrow radiation cone (dark red) with increased brilliance in comparison to the emission cone of a conventional anode (light red). The diamond forms the vacuum window and, at the same time, supports the waveguide structure, which can consist of cylindrical (**B**) or planar guides (**C**).

into just one waveguide mode $W_{if} = 2\pi/\hbar \,|\, H_{if} \,|^2 \delta(E_i - E_f)$ with dipolar interaction $H = -\boldsymbol{\mu} \cdot \mathbf{E}$ and waveguide modes of vector potential $A_m = c_m \exp(i\beta_m z)\psi_m(\boldsymbol{r}_\perp)$, the quantized field of the cavity mode becomes (*41*)

$$\mathbf{E}(\boldsymbol{r}_\perp, t) = \sum_m \sqrt{\frac{\hbar\omega_m}{2}} \left(i a_m e^{-i\omega t} \mathbf{A}_\mathbf{m}(\boldsymbol{r}_\perp) - i a_m^\dagger e^{i\omega t} \mathbf{A}_\mathbf{m}^*(\boldsymbol{r}_\perp) \right) \qquad (2)$$

We now consider the shape function of the guided mode $\psi_m(\boldsymbol{r}_\perp)$ in such a (planar or channel) waveguide. The mode intensity distribution $I_m \propto |\,\psi_m\,|^2$ has a width Δ that is smaller than the guiding channel cross section a because of the mode confinement but is on the same order. The modes are orthogonal and normalized

$$\int d\boldsymbol{r}_\perp \psi_m(\boldsymbol{r}_\perp)\, \psi_n^*(\boldsymbol{r}_\perp) = \delta_{nm} \qquad (3)$$

where the integral is in the plane orthogonal to the optical axis. At the waveguide exit, the mode propagates (diffracts) into free space with a divergence given by $\theta = c_a \lambda/\Delta$, where the prefactor c_a depends on the exact functional shape of the mode. θ can, of course, also be regarded as a numerical aperture, and Δ can be regarded as a resolution-defining beam confinement. Let the guiding core (or cladding) contain atoms in an excited state, for example, due to K-shell ionization following electron impact, and hence be a source of x-ray emission. Since the mode density differs from free space, the emission rate of x-ray photons is modified by the cavity. Analogous to the optical case, where 1d and 2d emission into cavity modes is well established (*42*), we can also use the Purcell factor here, generalized from 3d cavities to one- and two-dimensional resonators and set $n \simeq 1$ for hard x-rays. The enhancement factor for spontaneous emission into an x-ray waveguide mode then becomes (*43*)

$$\text{1d: } F_{1d} = \frac{\lambda}{4} \frac{Q_{planar}}{d_{eff}}$$

$$\text{2d: } F_{2d} = \frac{1}{\pi} \left(\frac{\lambda}{2} \right)^2 \frac{Q_{channel}}{A_{eff}}$$

for planar and channel waveguides, respectively. Here, Q is the quality factor of the cavity mode, which can be calculated for a leaky cavity by numerical field propagation based on the reciprocity relation. For this purpose, one computes the field intensity enhancement in the resonator, when a free-space solution impinges onto the resonator from infinity with suitable boundary conditions and under angles fulfilling the resonance condition. While plane wave solutions are used for the planar case, Bessel functions are suitable for the cylindrical waveguides, yielding typical values in the range of $Q_{planar} \simeq 10^1$ to 10^2 and $Q_{channel} \simeq 10^2$ to 10^4, depending on the parameters; see also (*44*) for calculations of Q in the analog case of optical waveguides. The effective confinement d_{eff} and A_{eff} is obtained from the mode intensity distribution $|\,\psi\,|^2$ and hence is approximately the width $\Delta < a$ of the mode. For the typical mode confinement of hard x-ray waveguides, we always have $(\lambda/a) \leq 10^{-2}$, so that emission into free space completely dominates the emission into the mode. However, compared to the photons emitted into the particular solid angle Ω_θ of the mode in the absence of the waveguide, we still can have a substantial gain, namely

$$G_{planar} = F_{1d} \frac{4\pi}{2\pi\,\theta} = \frac{1}{2\,c_a} Q_{planar} \frac{\Delta}{d_{eff}} = c_m\, Q_{planar} \qquad (4)$$

with unitless mode-specific prefactor $c_m = \Delta/(2c_a d_{eff})$. For a channel waveguide, we obtain the same relation with the corresponding Q factor and $c_m = \Delta^2/(c_a^2 A_{eff})$. Since $\Delta \approx d_{eff}$, the value of c_m is of order $O(1)$ and can be determined from precise numerical calculations, which can also take the distribution of the metal source atoms into account. As we see, the gain in the directional brilliance of the source, i.e., the brilliance measured when only the far-field radiation cone of the mode is evaluated, is essentially given by the quality factor of the waveguide; hence, $G \simeq Q$.

Last, we discuss the experimental Q factor of the waveguide resonators in the current work. Starting from the definition $Q = 2\pi E_0/E_L$, where E_0 denotes the stored energy and E_L denotes the lost energy per cycle in the waveguide resonator, we have to consider the exponential decay of the waveguide's exit intensity, as the generating e-beam is moved away from the edge, i.e., the curve measured in Fig. 5B. Expressed in number of cycles n_c, where a cycle is defined by one period of the internal total reflection of the guided beams, we

can write for the stored energy in the resonator $E_S = E_0 e^{-\mu n_c}$. Hence, $Q = 2\pi/\mu = 2\pi z_{1/e}/(2\Delta l)$, with $z_{1/e}$ as the 1/*e*-length of the decay and Δl as the distance between two consecutive reflections, calculated from the internal mode propagation angle θ_{int} and the effective width of the waveguide mode D_{eff}. With θ_{int} given by Snell's law and the external angle of the mode calculated from the Parratt formalism, Q can be directly computed from the measured $z_{1/e}$. From the biexponential fit in Fig. 5B, we obtain $z_{1/e} = 622(11)$ μm and $z_{1/e} = 82(2)$ μm, for the 0th and 1st mode, respectively, and hence, $Q_0 = 64(2)$ and $Q_1 = 11.0(3)$. The experimentally determined values for $z_{1/e}$ also indicate that a much higher photon number could have coupled into the waveguide mode by expanding the e-beam while keeping the x-ray source size constant. The width of the e-beam could be increased to the measured modal decay length $z_{1/e}$ (see Figs. 7 and 5). However, at the current setup, increasing the beam size and beam power was not possible for reasons of e-beam optics. Furthermore, it would have resulted in detector saturation. Conversely, a correspondingly upgraded experimental setup would directly result in the corresponding brilliance gain as shown in Fig. 7.

Summary and outlook

We showed the direct emission of spontaneous x-rays into waveguide modes, as a manifestation of the Purcell effect. As a result of this work, we demonstrated a novel x-ray source concept based on x-ray photon emission directly into x-ray waveguide modes. Instead of first generating a beam in an x-ray tube and then coupling it into an optic, photons are generated directly in a structured anode target, forming an x-ray waveguide or waveguide array. The metal for emission of characteristic radiation can be a component of the cladding or can be integrated into the guiding core. The simplest such structure is an array of planar waveguides deposited onto a substrate, which can be used either in reflection geometry, as was done in this work, or in transmission geometry [see Fig. 8 (B and C)]. If the geometry is properly chosen, then the size of the effective x-ray source spot does not depend on the e-beam spot size for the generation of x-rays in tabletop sources with waveguide anodes. This observation results in an estimated brilliance of $B \simeq 5 \times 10^{11}$ ph s^{-1} $mrad^{-2}mm^{-2}$ for a "fully filled" cavity (Fig. 7), operated at the presumed power threshold for solid targets. This will require a suitable heat management. Two-dimensional waveguide cavities could be realized by an array of channel waveguides, formed, for example, by macroscopically long cylindrical holes with radius $a \simeq 50$ to 200 nm etched into a metal. For these waveguide channels, the mode density calculations yield even higher mode densities and Q factors in the range of 10^3 to 10^4, depending on photon energy, optical constants of the materials, and geometric parameters. Directed emission of characteristic radiation and bremsstrahlung into waveguide modes along with an associated increase of spatial coherence in the corresponding angular cone could greatly benefit applications such as coherent imaging without the need for synchrotron radiation.

METHODS

Waveguide structures

In this work, we used three different waveguide systems (c.f. Table 1). Two systems (Fe/Ni and Mo/C multiwaveguides) were fabricated by magnetron sputtering by Incoatec GmbH (Geesthacht, Germany). The Fe/Ni system consists of 50 waveguides each with layer sequence of [Ni (10 nm)/C (24.5 nm)/Fe (1 nm)/C (24.5 nm)] deposited on a buffer layer of 30-nm Ni. The Mo/C system consists of 30 waveguides each with a layer sequence of [Mo (25 nm)/C (16 nm)/Mo (1 nm)/C (16 nm)] deposited on a layer of 30-nm Mo and an additional 10-nm-thick buffer layer of Cr. Both systems were deposited on a 3-mm-thick Si substrate. The third waveguide system is a single-waveguide Co/Cu system fabricated by pulsed laser deposition. The exact layer sequence is [Cu (5 nm)/C (20 nm)/Co (2 nm)/C (20 nm)/Cu (40 nm)] on 1-mm-thick Si substrate. The Mo/C and the Fe/Ni system were diced by a wafer saw (DAD321, DISCO, Tokyo, Japan); the Co/Cu waveguide was cut by scribe and break with a diamond tip. No further processing was done to the edges of the samples.

Cavity modes excited by synchrotron radiation

The experiments with synchrotron radiation were carried out at the GINIX endstation (*32*) of the beamline P10 at the PETRA III storage ring (DESY, Hamburg, Germany). The schematic of the experimental setup is shown in Fig. 1B. The 8-keV synchrotron beam was focused by a Kirkpatrick-Baez mirror system to about 500 nm by 350 nm [horizontal × vertical ($h \times v$)], with a divergence of 1.6 mrad by 1.0 mrad ($h \times v$).

Instead of the SDD detector and an entrance slit (Fig. 1A), we used the hybrid pixel area detector MÖNCH (see below) for the x-ray detection. The detector was placed at 90° to the incoming synchrotron beam. The distance between primary beam and detector was 200 mm. We used an interpolation factor of 5, resulting in a pixel size of 5 μm. Hence, the angular resolution $\Delta\theta_f$ of the observation angle θ_f is 25 μrad. The energy resolution of about 1 keV was sufficient to separate fluorescence and primary radiation, whereas it was not sufficient to separate K_α and K_β radiation. We used this setup in combination with the Co/Cu waveguide (c.f. fig. S2) and the Fe/Ni system (c.f. Fig. 4). The angle of grazing incidence θ_{in} of the synchrotron beam was 4.1 mrad for the Co/Cu and 7.6 mrad for the Fe/Ni waveguide. Note that in both systems with 8-keV primary radiation, only the central ∂-layer (Co and Fe) was excited, whereas the K-edge of the cladding material (Cu and Ni) is above the excitation energy.

Cavity modes excited at a μ-focus x-ray source

We used a liquid-metal jet μ-focus x-ray source (MetalJet D2, Excillum AB, Kista, Sweden) with Galinstan anode, operated at 70-kV acceleration voltage, a total power of 60 W, and an electron spot size of 6 μm by 10 μm ($h \times v$). The primary beam was focused by a Montel multilayer optic (ELM43GA, Incoatec GmbH, Geesthacht, Germany) to a spot size of 100 μm and a divergence of 7.5 mrad. The reflection of the focusing optic is optimized for the Ga-K_α radiation. A schematic of the setup is shown in Fig. 1B. The SDD detector (see below) was placed at 90° toward the primary beam. The distance between the detection entrance slit and the primary beam was 200 mm. The width of the entrance slit was $\Delta y = 50$ μm, resulting in an angular resolution $\Delta\theta_f$ of the observation angle θ_f of 250 μrad.

We used the Co/Cu waveguide at this setup (c.f. Fig. 3). In this experiment, the incoming Ga-K_α radiation excites fluorescence in both the Co ∂-layer and the Cu cladding.

Cavity modes excited with electron impact

We used the electron gun and electron optics of a μ-focus x-ray source (R5 liquid-metal jet prototype, Excillum AB, Kista, Sweden) with a customized anode chamber design. The chamber enables the mounting of planar waveguide structures as anode with orthogonal

electron impact onto the top surface of the waveguide. The e-beam was scanned along the waveguide's surface by the deflection coils of the electron optics. The following settings were used:

Co/Cu waveguide, 35-kV acceleration voltage, 450-mW e-beam power, SDD detector with 100-μm entrance slit, 350-mm source–to–detector-slit distance, $\Delta\theta_f \approx 285$ μrad angular resolution of detection angle, and 40-s exposure time (c.f. Fig. 3).

Fe/Ni waveguide (SDD detector), 15-kV acceleration voltage, 450-mW e-beam power, SDD detector with 50-μm entrance slit, 370-mm source–to–detector-slit distance, $\Delta\theta_f \approx 270$-μrad angular resolution of detection angle, and 10-s exposure time (c.f. Fig. 6).

Fe/Ni waveguide (MÖNCH detector), 15-kV acceleration voltage, 450-mW e-beam power, MÖNCH detector, 165-mm source-to-detector distance, 25-μm physical pixel size, 5-μm interpolated pixel size (5× interpolation), $\Delta\theta_f \approx 30.3$ μrad angular resolution of detection angle, 1-ms exposure time per frame, and 500,000 frames per e-beam position; a 20-μm-thick steel foil was used as chromatic filter (c.f. fig. S4).

Mo/C waveguide, 50-kV acceleration voltage, 400-mW e-beam power, MÖNCH detector, 250-mm source-to-detector distance, 25-μm physical pixel size, 6.25-μm interpolated pixel size (4× interpolation), $\Delta\theta_f \approx 25$ μrad angular resolution of detection angle, 1-ms exposure time per frame, and 500,000 frames per e-beam position. A 35-μm-thick Ag foil was used as chromatic filter to increase the contrast between the Mo-K_α/K_β radiation and the bremsstrahlung's background (c.f. Fig. 5).

Energy width and finesse (Mo/C waveguide)

For the Mo/C waveguide, we can calculate the energy width (FWHM) of the m-th resonant mode with photon energy E as $\delta E_m = \frac{E}{Q_m}$. With the previously determined Q factors for the 0th and 1st mode [$Q_0 = 64(2)$ and $Q_1 = 11.0(3)$], we get $\delta E_0 = 0.273(5)$ keV and $\delta E_1 = 1.60(4)$ keV. The energy linewidth (FWHM) of the characteristic Mo-K_α and K_β radiation is between 6 and 7 eV (*45*). The finesse of the waveguide is given by (*46*)

$$F = \frac{\pi}{2\arcsin\left(\frac{1-\sqrt{\rho}}{2\sqrt[4]{\rho}}\right)} \quad (5)$$

where ρ is the fraction of energy stored in the resonator after one full cycle. With $Q = 2\pi/\mu$ and $1/\mu$ as the number of cycles, where the fraction of energy in the resonator drops to $1/e$, we get $\rho = \exp(-\mu)$. Hence, the finesse is $F_0 = 65(2)$ and $F_1 \approx 11(1)$ for the 0th and 1st mode, respectively.

Detectors

We used two different detectors, an SDD and a hybrid-pixel area detector. The SDD detector (AXAS-M1 H50-139V, KETEK GmbH, Munich, Germany) has a single pixel with a detection area of 65 mm^2, 450-μm sensor thickness, and a built-in 100-mm-long multilayer collimator. The energy resolution is specified to be 139 eV (FWHM) at 5.9 keV. To increase the angular resolution of the SDD detector, we used slit blades in front of the built-in collimator. We mounted the detector on a motorized stepper stage enabling the acquisition of angular dependent intensity measurements.

As a second detector, we used the MÖNCH03 prototype detector (*31*), developed at the Paul Scherrer Institute (Villigen, Switzerland). The MÖNCH is a charge-integrating hybrid-pixel area detector with 25-μm physical pixel size and a number of 400 × 400 pixels. By counting single-photon events within an area of 3 × 3 pixels, we are able to access the deposited charge distribution of each individual photon. This enabled the calculation of the photon energy, which is proportional to the deposited charge and to interpolate the exact photon hit position with subpixel accuracy (*47*). In this work, we used an interpolation factor of 5, resulting in an interpolated pixel size of 5 μm. The theoretical energy resolution is 0.85 keV; in this experiment, we observed an energy resolution of about 1 keV (FWHM).

Calculation of radiant flux and brilliance

We calculated the radiant flux of the Co/Cu waveguide (c.f. Fig. 3 and fig. S1) from the photon counts of the SDD detector. The air absorption of the path between source and detector is corrected, with a transmission of about 55% for Co-K_α, 64% for Co-K_β, and 66% for Cu-K_α (*48*). The solid angle of the detector is given by the detection area 0.8 mm^2 (slit gap × sensor width) and the source-to-detector distance (350 mm).

The Mo-K radiant flux Φ_p and brilliance B_p of the Mo/C waveguide (c. f. Fig. 5) are calculated from the registered photon counts on the MÖNCH detector. The counts are corrected by the absorption of the 35-μm-thick Ag filter, with a transmission of about 38% at 17.5 keV (*48*). Furthermore, the absorption cross section of the 300-μm-thick Si sensor of the MÖNCH is corrected. The absorption of the sensor is about 37% at 17.5 keV (*48*). The solid angle of a single pixel is given by the pixel size and source-to-detector distance. For the calculation of the source brilliance B_p exiting through the truncated side face of the Mo/C multiwaveguide system, we estimated the effective x-ray source spot size to be given by the guiding layer thickness times the number of waveguides 33 nm × 30 in the y direction and the spot size of the e-beam (10 μm, FWHM) in the lateral direction. Hence, the size of the effective x-ray source spot is $A_{source} \approx 9.9\ \mu m^2$.

Finite-difference simulation

We used PyPropagate (*34*) for simulating the propagation of the electromagnetic field inside the waveguide cavities. The angular-dependent intensity maps were calculated using the reciprocity theorem (c.f. Fig. 2). Hence, we used PyPropagate to calculate the internal field inside the waveguide at a given position $I_{\theta_{PW}}(y, \Delta z)$ for different angles of plane wave incidence θ_{PW}. According to the reciprocity theorem, these intensities correspond to the observed angular intensity distribution if a molecule emits photons at the given position (y, Δz).

SUPPLEMENTARY MATERIALS

Supplementary material for this article is available at http://advances.sciencemag.org/cgi/content/full/7/4/eabd5677/DC1

REFERENCES AND NOTES

1. R. Behling, *Modern Diagnostic X-ray Sources* (CRC Press, 2016).
2. O. Hemberg, M. Otendal, H. M. Hertz, Liquid-metal-jet anode electron-impact x-ray source. *Appl. Phys. Lett.* **83**, 1483–1485 (2003).
3. M. Otendal, T. Tuohimaa, U. Vogt, H. M. Hertz, A 9keV electron-impact liquid-gallium-jet x-ray source. *Rev. Sci. Instrum.* **79**, 016102 (2008).
4. Y. V. Shvyd'ko, M. Lerche, H.-C. Wille, E. Gerdau, M. Lucht, H. D. Rüter, E. E. Alp, R. Khachatryan, X-ray interferometry with microelectronvolt resolution. *Phys. Rev. Lett.* **90**, 013904 (2003).
5. S.-L. Chang, Y. P. Stetsko, M.-T. Tang, Y.-R. Lee, W.-H. Sun, M. Yabashi, T. Ishikawa, X-ray resonance in crystal cavities: Realization of Fabry-Perot resonator for hard x rays. *Phys. Rev. Lett.* **94**, 174801 (2005).
6. Y. V. Shvyd'ko, S. Stoupin, A. Cunsolo, A. H. Said, X. Huang, High-reflectivity high-resolution x-ray crystal optics with diamonds. *Nat. Phys.* **6**, 196–199 (2010).

7. A. Halavanau, A. Benediktovitch, A. A. Lutman, D. DePonte, D. Cocco, N. Rohringer, U. Bergmann, C. Pellegrini, Population inversion x-ray laser oscillator. *Proc. Natl. Acad. Sci. U.S.A.* **117**, 15511–15516 (2020).
8. K. H. Drexhage, H. Kuhn, F. P. Schäfer, Variation of the fluorescence decay time of a molecule in front of a mirror. *Ber. Bunsen. Phys. Chem* **72**, 329 (1968).
9. E. M. Purcell, Spontaneous emission probabilities at radio frequencies. *Phys. Rev.* **69**, 681 (1946).
10. W. Kossel, V. Loeck, H. Voges, Die Richtungsverteilung der in einem Kristall entstandenen charakteristischen Rontgenstrahlung. *Zeitschrift für Physik* **94**, 139–144 (1935).
11. P. Jonnard, J.-M. Ândré, C. Bonnelle, F. Bridou, B. Pardo, Modulation of x-ray line intensity emitted by a periodic structure under electron excitation. *Appl. Phys. Lett.* **81**, 1524–1526 (2002).
12. A. E. Kaplan, C. T. Law, P. L. Shkolnikov, X-ray narrow-line transition radiation source based on low-energy electron beams traversing a multilayer nanostructure. *Phys. Rev. E* **52**, 6795–6808 (1995).
13. J.-M. André, P. Jonnard, X-ray spontaneous emission control by 1-dimensional photonic bandgap structure. *Eur. Phys. J. D* **57**, 411–418 (2010).
14. V. Kaplin, V. Sohoreva, S. Uglov, O. Bulaev, A. Voronin, M. Piestrup, C. Gary, X-rays generated by relativistic electrons in a waveguide radiator mounted inside a betatron. *Nucl. Instr. Meth. Phys. Res. B* **269**, 1518–1522 (2011).
15. E. Spiller, A. Segmüller, Propagation of x rays in waveguides. *Appl. Phys. Lett.* **24**, 60–61 (1974).
16. Y. P. Feng, S. K. Sinha, H. W. Deckman, J. B. Hastings, D. P. Siddons, X-ray flux enhancement in thin-film waveguides using resonant beam couplers. *Phys. Rev. Lett.* **71**, 537–540 (1993).
17. S. Lagomarsino, A. Cedola, P. Cloetens, S. Di Fonzo, W. Jark, G. Soullie, C. Riekel, Phase contrast hard x-ray microscopy with submicron resolution. *Appl. Phys. Lett.* **71**, 2557–2559 (1997).
18. M. J. Zwanenburg, J. F. Peters, J. H. H. Bongaerts, S. A. de Vries, D. L. Abernathy, J. F. van der Veen, Coherent propagation of x rays in a planar waveguide with a tunable air gap. *Phys. Rev. Lett.* **82**, 1696–1699 (1999).
19. F. Pfeiffer, T. Salditt, P. Høghøj, I. Anderson, N. Schell, X-ray waveguides with multiple guiding layers. *Phys. Rev. B* **62**, 16939–16943 (2000).
20. F. Pfeiffer, C. David, M. Burghammer, C. Riekel, T. Salditt, Two-dimensional x-ray waveguides and point sources. *Science* **297**, 230–234 (2002).
21. A. Jarre, C. Fuhse, C. Ollinger, J. Seeger, R. Tucoulou, T. Salditt, Two-dimensional hard x-ray beam compression by combined focusing and waveguide optics. *Phys. Rev. Lett.* **94**, 074801 (2005).
22. H.-Y. Chen, S. Hoffmann, T. Salditt, X-ray beam compression by tapered waveguides. *Appl. Phys. Lett.* **106**, 194105 (2015).
23. S. P. Krüger, H. Neubauer, M. Bartels, S. Kalbfleisch, K. Giewekemeyer, P. J. Wilbrandt, M. Sprung, T. Salditt, Sub-10 nm beam confinement by x-ray waveguides: Design, fabrication and characterization of optical properties. *J. Synchrotron. Radiat.* **19**, 227–236 (2012).
24. R. Röhlsberger, K. Schlage, T. Klein, O. Leupold, Accelerating the spontaneous emission of x rays from atoms in a cavity. *Phys. Rev. Lett.* **95**, 097601 (2005).
25. R. Röhlsberger, K. Schlage, B. Sahoo, S. Couet, R. Rüffer, Collective lamb shift in single-photon superradiance. *Science* **328**, 1248–1251 (2010).
26. R. Röhlsberger, H.-C. Wille, K. Schlage, B. Sahoo, Electromagnetically induced transparency with resonant nuclei in a cavity. *Nature* **482**, 199–203 (2012).
27. J. Haber, K. S. Schulze, K. Schlage, R. Loetzsch, L. Bocklage, T. Gurieva, H. Bernhardt, H.-C. Wille, R. Rüffer, I. Uschmann, G. G. Paulus, R. Röhlsberger, Collective strong coupling of x-rays and nuclei in a nuclear optical lattice. *Nat. Photonics* **10**, 445–449 (2016).
28. J. Haber, J. Gollwitzer, S. Francoual, M. Tolkiehn, J. Strempfer, R. Röhlsberger, Spectral control of an x-ray L-edge transition via a thin-film cavity. *Phys. Rev. Lett.* **122**, 123608 (2019).
29. M. Bartels, M. Krenkel, J. Haber, R. N. Wilke, T. Salditt, X-ray holographic imaging of hydrated biological cells in solution. *Phys. Rev. Lett.* **114**, 048103 (2015).
30. Y. I. Dudchik, F. F. Komarov, Y. A. Kostantinov, in *X-ray and Ultraviolet Sensors and Applications* (SPIE, 1995), vol. 2519, pp. 50–59.
31. M. Ramilli, A. Bergamaschi, M. Andrae, M. Brückner, S. Cartier, R. Dinapoli, E. Fröjdh, D. Greiffenberg, T. Hutwelker, C. Lopez-Cuenca, D. Mezza, A. Mozzanica, M. Ruat, S. Redford, B. Schmitt, X. Shi, G. Tinti, J. Zhang, Measurements with MÖNCH, a 25 μm pixel pitch hybrid pixel detector. *J. Instrum.* **12**, C01071 (2017).
32. T. Salditt, M. Osterhoff, M. Krenkel, R. Wilke, M. Priebe, M. Bartels, S. Kalbfleisch, M. Sprung, Compound focusing mirror and x-ray waveguide optics for coherent imaging and nano-diffraction. *J. Synchrotron Radiat.* **22**, 867–878 (2015).
33. L. G. Parratt, Surface studies of solids by total reflection of x-rays. *Phys. Rev.* **95**, 359–369 (1954).
34. L. Melchior, T. Salditt, Finite difference methods for stationary and time-dependent x-ray propagation. *Opt. Express* **25**, 32090–32109 (2017).
35. W. Jark, S. Di Fonzo, Prediction of the transmission through thin-film waveguides for x-ray microscopy. *J. Synchrotron Radiat.* **11**, 386–392 (2004).
36. F. Salvat, *OECD NEA Data Bank, NEA/NSC/DOC(2015)3* (2015).
37. K. P. Heeg, C. Ott, D. Schumacher, H.-C. Wille, R. Röhlsberger, T. Pfeifer, J. Evers, Interferometric phase detection at x-ray energies via Fano resonance control. *Phys. Rev. Lett.* **114**, 207401 (2015).
38. M. F. Limonov, M. V. Rybin, A. N. Poddubny, Y. S. Kivshar, Fano resonances in photonics. *Nat. Photonics* **11**, 543–554 (2017).
39. D. Lentrodt, K. P. Heeg, C. H. Keitel, J. Evers, Ab initio quantum models for thin-film x-ray cavity QED. *Phys. Rev. Research* **2**, 023396 (2020).
40. K. M. Schulz, D. Jalas, A. Y. Petrov, M. Eich, Reciprocity approach for calculating the Purcell effect for emission into an open optical system. *Opt. Express* **26**, 19247–19258 (2018).
41. B. J. Dalton, E. S. Guerra, P. L. Knight, Field quantization in dielectric media and the generalized multipolar Hamiltonian. *Phys. Rev. A* **54**, 2292–2313 (1996).
42. Y. C. Jun, R. M. Briggs, H. A. Atwater, M. L. Brongersma, Broadband enhancement of light emission in silicon slot waveguides. *Opt. Express* **17**, 7479–7490 (2009).
43. R. S. Tummidi, R. M. Pafchek, K. Kim, T. L. Koch, in *2009 6th IEEE International Conference on Group IV Photonics* (2009), pp. 226–228.
44. S. D. Brorson, *Electromagnetic Field Mode Density Calculated via Mode Counting* (CRC Press, 1995).
45. M. H. Mendenhall, L. T. Hudson, C. I. Szabo, A. Henins, J. P. Cline, The molybdenum K-shell x-ray emission spectrum. *J. Phys. B* **52**, 215004 (2019).
46. R. Paschotta, *Encyclopedia of Laser Physics and Technology* (Wiley-VCH, ed. 1, 2008).
47. S. Cartier, A. Bergamaschi, R. Dinapoli, D. Greiffenberg, I. Johnson, J. H. Jungmann, D. Mezza, A. Mozzanica, B. Schmitt, X. Shi, M. Stampanoni, J. Sun, G. Tinti, Micron resolution of MÖNCH and GOTTHARD, small pitch charge integrating detectors with single photon sensitivity. *J. Instrum.* **9**, C05027 (2014).
48. T. Schoonjans, A. Brunetti, B. Golosio, M. Sanchez del Rio, V. A. Solé, C. Ferrero, L. Vincze, The xraylib library for x-ray–matter interactions. Recent developments. *Spectrochim. Acta B* **66**, 776–784 (2011).

Acknowledgments: We thank S. Hoffmann-Urlaub for preparation of the thin-film sample by pulsed laser deposition, A. Bergamaschi and S. Chiriotti for letting us use the MÖNCH detector and for advice on its use, and M. Osterhoff and L. M. Lohse for help in implementing the detection scheme. **Funding:** We acknowledge funding by the Max Planck School of Photonics supported by BMBF, Max Planck Society, and Fraunhofer Society. **Author contributions:** Both authors designed research together. In-house experiments were carried out by M.V.; synchrotron experiments were carried out by both authors. M.V. performed data analysis and simulation in close discussion and interaction with T.S. Both authors wrote the manuscript. **Competing interests:** M.V. and T.S. are inventors on a pending patent related to this work filed by Georg-August-Universität Göttingen (no. DE10 2020 109 906.1, filed April 2020). The authors declare that they have no other competing interests. **Data and materials availability:** All data needed to evaluate the conclusions in the paper are present in the paper and/or the Supplementary Materials. Additional data related to this paper may be requested from the authors.

Submitted 29 June 2020
Accepted 4 December 2020
Published 22 January 2021
10.1126/sciadv.abd5677

Citation: M. Vassholz, T. Salditt, Observation of electron-induced characteristic x-ray and bremsstrahlung radiation from a waveguide cavity. *Sci. Adv.* **7**, eabd5677 (2021).

Observation of electron-induced characteristic x-ray and bremsstrahlung radiation from a waveguide cavity

Malte Vassholz and Tim Salditt

Sci Adv **7** (4), eabd5677.
DOI: 10.1126/sciadv.abd5677